Applied Physics Letters

Adaptive light-sheet fluorescence microscopy with a deformable mirror for video-rate volumetric imaging

Cite as: Appl. Phys. Lett. **121**, 193703 (2022); https://doi.org/10.1063/5.0125946
Submitted: 14 September 2022 • Accepted: 25 October 2022 • Published Online: 10 November 2022
Published open access through an agreement with JISC Collections

Wenzhi Hong, Terry Wright, Hugh Sparks, et al.

Applied Physics Letters ARTICLE scitation.org/journal/apl

Adaptive light-sheet fluorescence microscopy with a deformable mirror for video-rate volumetric imaging

Cite as: Appl. Phys. Lett. **121**, 193703 (2022); doi: 10.1063/5.0125946
Submitted: 14 September 2022 · Accepted: 25 October 2022 ·
Published Online: 10 November 2022

Wenzhi Hong,[1] Terry Wright,[1] Hugh Sparks,[1] Liuba Dvinskikh,[1] Ken MacLeod,[2] Carl Paterson,[1] and Chris Dunsby[1,a)]

AFFILIATIONS

[1]Photonics Group, Physics Department, Imperial College London, London, United Kingdom
[2]Myocardial Function Section, National Heart and Lung Institute, Imperial College London, London, United Kingdom

Note: This paper is part of the APL Special Collection on Advances in Optical Microscopy for Bioimaging.
[a)]**Author to whom correspondence should be addressed:** christopher.dunsby@imperial.ac.uk

ABSTRACT

Light-sheet fluorescence microscopy (LSFM) achieves optically sectioned imaging with the relatively low photobleaching and phototoxic effect. To achieve high-speed volumetric LSFM imaging without perturbing the sample, it is necessary to use some form of remote refocusing in the detection beam path. Previous work used electrically tunable lenses, tunable acoustic gradient index of refraction lenses, or the remote-refocusing approach of Botcherby *et al.* [Opt. Lett. **32**(14), 2007 (2007)] to achieve remote refocusing. However, these approaches generally only provide low-order defocus correction, which is not compatible with higher-NA objectives that require higher order defocus corrections or reduce the optical throughput. In order to simultaneously achieve high-speed remote refocusing and correct system aberrations, we employ a deformable mirror in the detection path that is capable of providing higher orders of defocus and aberration correction in an optical system with an NA of 0.72–0.75. We demonstrate high-speed volumetric imaging at 26.3 volumes per second and 35 frames per volume for a defocus range of −50 to 50 μm.

Compared to conventional fluorescence microscopies, light-sheet fluorescence microscopy (LSFM) can provide faster fluorescence imaging with lower phototoxicity and photobleaching by generating a thin sheet of light to scan through the sample.[1] In order to achieve high-speed three-dimensional (3D) imaging in an LSFM system without mechanically perturbing the sample, various methods for remote refocusing have been applied. Remote refocusing can be achieved by employing a pair of microscopes placed back-to-back to generate an undistorted intermediate image, which can then be scanned by an adjustable tertiary microscope to achieve volumetric imaging.[2] A folded version of this approach has previously been applied to refocusing in LSFM, but the use of a polarizing beam splitter (BS) reduces the optical throughput.[3] Another method is to use adaptive optics devices to generate converging or diverging wavefronts at the pupil plane to achieve refocusing. Previous work has employed electrically tunable lenses (ETL)[4] and tunable acoustic gradient index of refraction lenses (TAG lenses)[5] to provide low-order quadratic primary defocus to achieve remote refocusing. However, in LSFM systems with high-NA objectives, these devices are no longer suitable to provide the higher-order defocus terms necessary to achieve aberration-free remote refocusing or to compensate system aberrations. For example, for an NA of 0.75, low-order quadratic defocus alone only provides a diffraction-limited refocusing range of 22 μm with a water immersion objective, see Fig. 1 of Ref. 6.

In order to achieve high-speed remote refocusing while also correct the system aberrations in the LSFM, it is necessary to employ more complex adaptive optics devices such as deformable mirrors (DMs) or spatial light modulators (SLMs) in the system. Adaptive remote focusing with a DM has been previously demonstrated in multi-photon microscope systems.[7,8] A remote-refocusing system achieving video-rate refocusing with a DM was presented in Ref. 6. A LSFM system in Ref. 9 with a DM was developed for correcting aberrations in tissue cleared porcine cochleae imaging. Recently, another multi-photon microscope system was also developed with

both conjugate adaptive optics and remote refocusing for deep tissue imaging through mouse skull.[10] Although adaptive optics has been applied in LSFM systems for biomedical imaging, no adaptive LSFM system has yet been demonstrated to achieve high-speed remote refocusing and aberration-corrected volumetric imaging.

We previously demonstrated a method for achieving remote-refocusing using a membrane DM.[6] Here, we build on this work, applying it to remote-refocusing of the detection arm of a LSFM system and achieve high-speed volumetric imaging at 26.3 volumes per second and with 35 frames per volume (920.5 fps) for a defocus range of -50 to 50 μm. We demonstrate the capabilities of the system by imaging static sunflower pollen grains and dynamic cardiomyocytes.

The configurations used for the optimization and imaging modes of the high-speed adaptive LSFM are shown in Fig. 1. In the optimization mode [Fig. 1(a)], a star test mask (STM) consisting of a hexagonal array of 1 μm diameter pinholes with 20 μm spacing on a hexagonal grid is placed in the front focal plane of the detection objective O1 (40×, 0.8 NA) using a custom mount ($\alpha = 50°$ to the optical table) that allows switching between the optimization and imaging modes without changing the position of objective O1 [see Fig. 1(b)]. The STM is transilluminated by an LED, the pupil of O1 is imaged to the DM via a 4-f relay, and the image of the STM recorded on an sCMOS camera. A fold angle introduced by the DM of $\theta = 34°$ is set to provide enough space for a Shack–Hartmann wavefront sensor-based DM flattening system [see Fig. 1(c)]. The DM pupil (13.5 mm) and the folding angle reduce the imaging NA from 0.8 to 0.75 (vertical) and 0.72 (horizontal).

When switching to the imaging mode [Fig. 1(d)], the STM, LED, and custom mount are removed. An emission filter (EF, SEM-FF03-525/50-25, Semrock or ET630/75M, Chroma) is added in front of the camera to block excitation light, and the illumination objective O2 is installed onto its mount. A sample stage is then placed beneath O1 and O2 to hold the glass slide and samples, and the optical axes of O1 and O2 are at 90° to one another [Fig. 1(e)]. Further details of the optical setup are given in the supplementary material Sec. 2.

The deformable mirror (DM97-15, Alpao) was selected due to its relatively large stroke (specified peak-to-valley mechanical motion of 30 μm for tip/tilt) and relatively high first resonance frequency (800 Hz). It is supplied with a default factory-measured influence matrix, so applying the zero actuator command vector to the DM will put it into its nominal factory-flat pose. However, the performance and response of the mirror depend on temperature,[11] and, thus, it is necessary to further flatten the DM to find its best flat before each optimization and imaging session.

An iterative algorithm using wavefront measurements from the Shack–Hartmann wavefront sensor (SHWS) (see the supplementary material Sec. 3) was used to optimize the flatness of the DM. This achieved an RMS wavefront error of 0.018 ± 0.001 μm ($n = 10$), which is smaller than the diffraction limit of 0.039 μm [corresponding to a Strehl ratio of 0.8 for a wavelength of 550 nm (Ref. 12)]. After the DM flattening process, the best flat command signal was saved for later DM optimization or sample imaging.

To achieve high-speed remote refocusing and minimize thermal and viscoelastic creep effects, the DM was oscillated continuously [Fig. S1(b)] with a sawtooth variation of defocus over time (see the supplementary material Sec. 4). The initial mirror poses were generated using the optical path difference (OPD) (relative to zero defocus) of high-NA defocus introduced in Refs. 2 and 6,

$$\mathrm{OPD}_{\mathrm{high}_{\mathrm{NA}}} = z\sqrt{n^2 - \mathrm{NA}^2 r^2}, \tag{1}$$

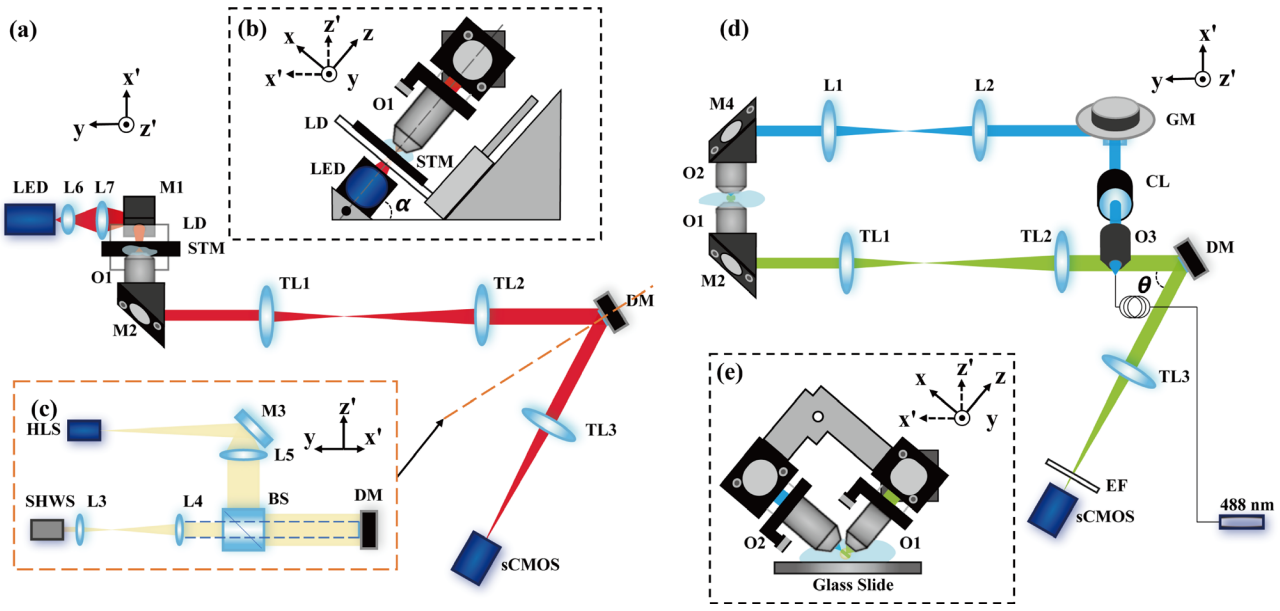

FIG. 1. Configurations of the optimization mode and imaging mode of the high-speed adaptive LSFM. (a) Schematic (top view) of the optimization mode. (b) The actual orientation of O1 and LED viewed end on. (c) Schematic (section view) of the DM flattening setup. (d) Schematic (top view) of the imaging mode including illumination and imaging parts. (e) The actual orientation of O1 and O2 viewed end on. O, objective; TL, tube lens; M, mirror; L, lens; LD, Lambertian diffuser; STM, star test mask; DM, deformable mirror; HLS, halogen light source; BS, beam splitter; SHWS, Shack–Hartmann wavefront sensor; GM, galvo mirror; and EF, emission filter.

where n is the refractive index in sample, NA is the actual imaging numerical aperture, z is the axial displacement from the objective focal plane to the defocus object, and r is the normalized radial pupil coordinate.

The initial mirror poses were then optimized following the method reported in Ref. 6 based on an image evaluation—instead of a wavefront sensor—with the STM used as the optimization object. The method used for calculation of the Strehl metric for each star in the image of the STM is described in the supplementary material Sec. 4. Rather than optimizing the mirror pose for every defocus position, 11 major poses on the outward sweep (corresponding to defocus positions from 50 to $-50\,\mu$m with $10\,\mu$m interval) were optimized, with 38 intermediate sub-poses between each major pose being calculated by linear interpolation. Considering the double-pass effect of the DM and the maximum OPD required for the high-NA defocus, the maximum mechanical peak-to-valley DM stroke required was $\sim 5.3\,\mu$m.[2] This approach of only optimizing the major poses together with linear interpolation between major poses aims to achieve a smooth movement of the DM through the scan range while keeping the time required for DM optimization to a reasonable duration. For each major pose, the amplitudes of high-NA defocus adjustment and Zernike modes Z4 to Z18 (see Table S1) were optimized to provide defocus and correct system aberrations at each defocus position. The high-NA defocus term was included to account for experimental error in positioning the STM. Therefore, the optical path difference introduced by the DM can be described by

$$\mathrm{OPD}_{\mathrm{DM}} = \mathrm{OPD}_{\mathrm{high_{NA}}}(z+a) + \sum_{i=4}^{18} b_i Z_i(r), \tag{2}$$

where z is the defocus position, a is the amplitude of high NA defocus adjustment, and b_i is the amplitude of the ith Zernike mode Z_i.[13] Return of the DM to the starting position was performed with four major poses with $20\,\mu$m interval from -50 to $50\,\mu$m; these major poses were not optimized (see the supplementary material Sec. 4). Only the front part of the DM sweep (from 50 to $-50\,\mu$m with $10\,\mu$m interval) was used for imaging.

Since the illumination objective O2 is removed while performing the DM optimization—so that there is sufficient space to place the STM near to O1—when switching to the LSFM imaging mode, it is necessary to then align the light sheet, so the illumination beam waist is at the center of the camera's field of view (FOV). To achieve this, a fluorescein solution ($5\,\mu$M, 46955, Fluka) was imaged with the DM best flat to produce an image of the edge of the fluorescein solution, where it meets the glass slide underneath [see Fig. S2(b)]. The illumination beam waist position was adjusted by moving O2 axially to produce the sharpest edge image at the center of FOV.

In order to achieve high-speed remote refocusing, a galvo mirror calibration is required to obtain the relationship between the illumination plane position and the galvo mirror voltage. The best flat was also applied on the DM in this calibration process. A series of voltages (from -0.56 to -0.44 V, manually chosen to cover the refocus range required) were then applied to the galvo mirror, which produced different illumination plane positions from the focal plane of O1 leading to displacements of the image of the edge. The position of the edge was determined from each image and used to calculate the corresponding defocus position. In each image, the intersection of the fluorescence edge was determined along three horizontal lines [see Fig. S2(b)] via Canny edge detection.[14] The defocus position z of the illumination sheet relative to the focal plane of the detection objective O1 can then be found by

$$z = \frac{p \times (x - x_0) \times \cos(\alpha)}{\mathrm{M}}, \tag{3}$$

where p is the pixel size, x_0 is the edge position when it is in the focal plane of O1, x is the moved edge position, α is the imaging objective angle shown in Fig. 1(b), and M is the system magnification (22.2×). All of the sampling points were calculated for their defocus positions, which produced a linear relationship between the defocus position and the galvo mirror voltage. A linear fit was then performed to generate an expression [see Fig. S2(a)] that can be used to control the galvo mirror during high-speed adaptive LSFM imaging.

All studies were carried out with the approval of the local Imperial College London ethical review board and the Home Office, UK, in accordance with the Animals (Scientific Procedures) Act 1986 Amendment Regulations 2012, and EU directive 2010/63/EU, which conforms to the Guide for the Care and Use of Laboratory Animals published by the U.S. National Institutes of Health under assurance number A5634–01.

In this paper, a sunflower pollen grain sample and live cardiomyocytes were prepared to show the system volumetric imaging performance for static and dynamic biological samples. The sunflower pollen grains were embedded in 1% agarose and cooled to form a volumetric sample. For live imaging of a dynamic sample, left ventricle myocytes, isolated from a male rat following the method outlined in Ref. 15, were labeled with a cell-permeant calcium indicator Fluo-4 AM (ThermoFisher Scientific) and cell mask orange (CMO) plasma membrane stain (ThermoFisher Scientific) according to the live-cell dual labeling and imaging preparation protocol described in Refs. 3 and 16. Full details are given in the supplementary material Sec. 6.

Details of the imaging modes used are given in the supplementary material Sec. 7. All of the Zernike modes from Z4 to Z18 (see Table S1) were used in the optimized DM pose command, and the corresponding amplitudes are shown in Fig. 2(a). It shows that although low order Zernike modes play a dominant role in the refocusing and aberration correction, the high order terms are also useful and important in high-speed DM optimization.

Strehl maps (a Voronoi diagram that assigned the estimated Strehl ratio of each pinhole to its nearest pixels, see the supplementary material Sec. 4 for the estimation of Strehl ratio) at different axial distances from the optimized defocus positions were measured by adding small displacements (from -1.5 to $-1.5\,\mu$m) when a pose for an optimized defocus position was applied on the DM, and the results are shown in Fig. 2(c). The maximum Strehl ratios in Fig. 2(b) were obtained from the central region ($200 \times 200\ \mu\mathrm{m}^2$) in the best Strehl maps in Fig. 2(c) and show the best performance achieved within this region. The mean Strehl ratios in Fig. 2(b) were calculated from the central region ($200 \times 200\ \mu\mathrm{m}^2$) of the $0\,\mu$m displacement Strehl maps in Fig. 2(c), which illustrate the performance of the system over the plane illuminated by the light sheet. As seen in Fig. 2(b), the DM dynamic optimization achieved a maximum Strehl ratio >0.8 over the range -20 to $40\,\mu$m and a mean Strehl ratio above 0.6 over the whole refocus range (from 50 to $-50\,\mu$m). Since the DM can be affected by temperature,[11] another evaluation (48 h after optimization) of the

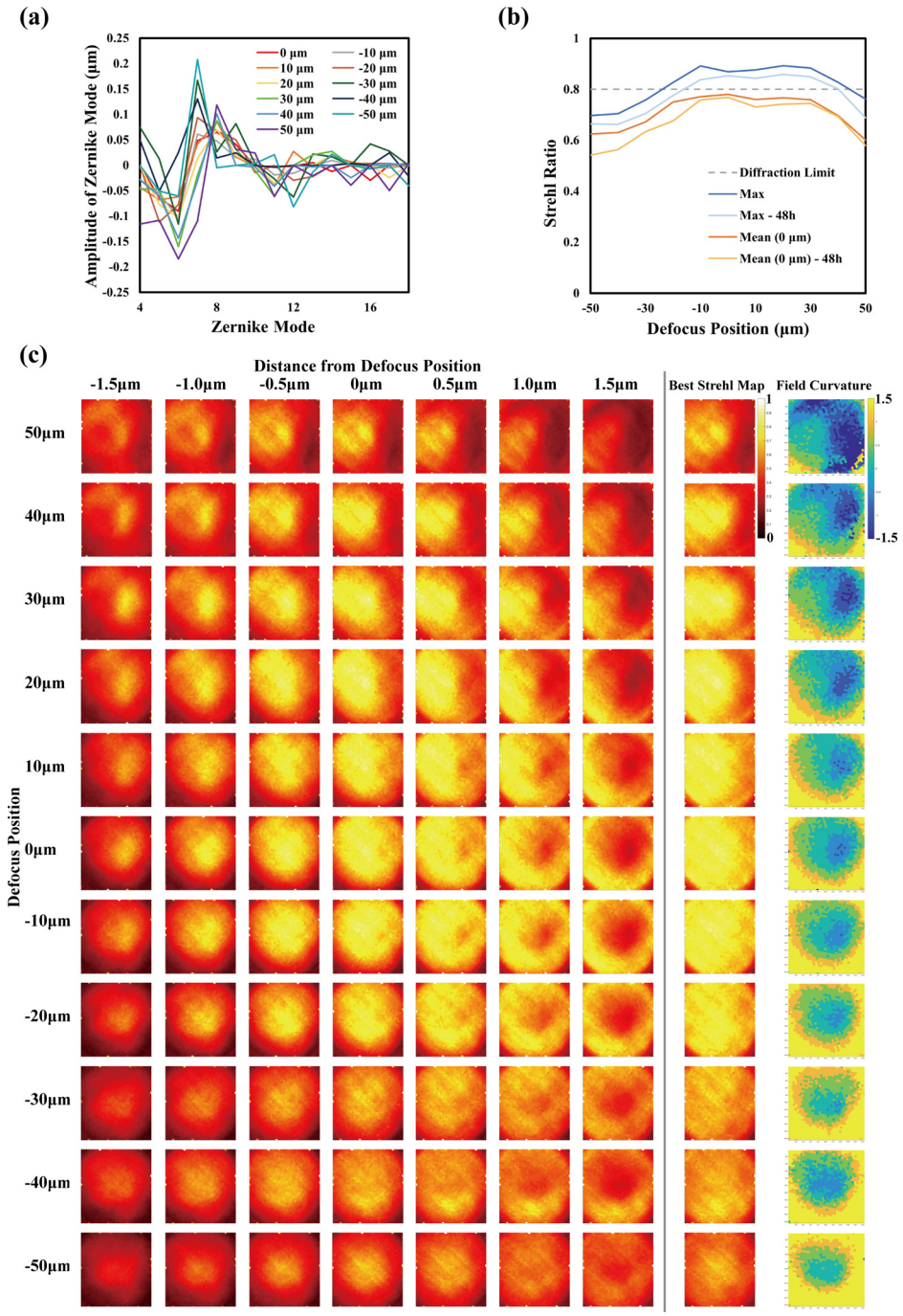

FIG. 2. Optimization results of the DM dynamic optimization. (a) The amplitudes of different Zernike modes from Z4 to Z18 at different optimized defocus positions. (b) The maximum Strehl ratios (see supplementary material Sec. 4) obtained from the central $200 \times 200\ \mu m^2$ region of the best Strehl maps at different optimized defocus positions, and mean Strehl ratios obtained from the central $200 \times 200\ \mu m^2$ region of the $0\ \mu m$ displacement Strehl maps at different optimized defocus positions. Data obtained immediately after and 48 h after optimization. (c) Strehl maps ($600 \times 600\ \mu m^2$) at different distances from the optimized defocus positions, which were used to generate the best Strehl maps and field curvature projections shown in the righthand two columns, respectively (see the supplementary material Sec. 8).

same set of optimized DM pose command was performed to test the optimization durability. The results show that the performance of the system only dropped by ~5% over this time period.

To characterize the high-speed adaptive LSFM system, a sample of fluorescent beads (250 nm actual diameter, 1:20 dilution in agarose) was imaged with the low-speed imaging mode volumetrically at the full sCMOS frame size, see the supplementary material Sec. 9 for methods. The results can be seen in Table S2. The system resolution was measured to be $0.51 \pm 0.04\ \mu m$ laterally (average over all defocus positions) and $2.24 \pm 0.32\ \mu m$ axially. The measured sectioning strength ($3.71 \pm 0.27\ \mu m$) compared well with the estimated theoretical light-sheet thickness. Further details are given in the supplementary material Sec. 10.

To demonstrate the system performance in imaging a static sample with the full frame of the sCMOS camera, a sunflower pollen grain

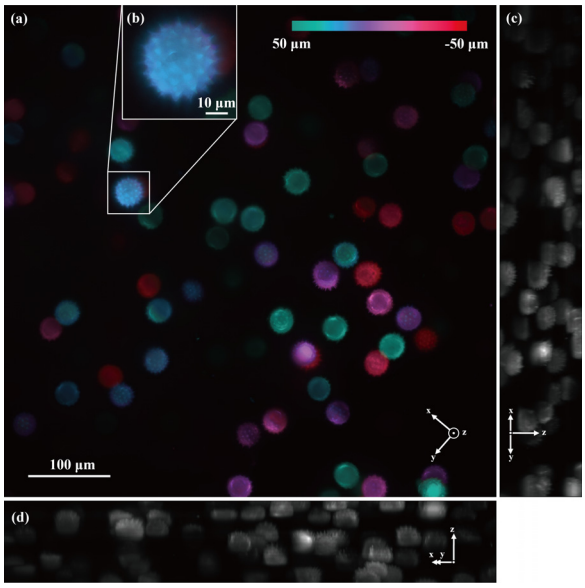

FIG. 3. (a) A color-coded 3D projection of pollen images from 50 to −50 μm. An averaged dark frame was subtracted from each frame prior to taking the projection. (b) A zoom-in image of a pollen grain. (c) and (d) The maximum intensity projections of (a) from the left and top, respectively.

sample was imaged with the low-speed imaging mode volumetrically from 50 to −50 μm with 1 μm interval. The color-coded 3D projection of the pollen images can be seen in Fig. 3. The inset in Fig. 3(b) shows the detail of the pollen structure. Figures 3(c) and 3(d) are, respectively, the maximum intensity projections of the pollen volume from the left and top.

The high-speed adaptive LSFM system was applied to image dynamic events in cardiomyocytes in 3D with the high-speed imaging mode. The cardiomyocytes were electrically paced to induce contraction using an applied pulse amplitude of 20 V with a pacing interval of 2 s (0.5 Hz) and 2 ms pulse duration. The electrical pacing induced calcium release leading to a global increase in Fluo-4 fluorescence intensity within the cells. This can be seen in Fig. 4(a), which shows selected z′-planes from the reconstructed volume (left to right) at selected time points (top to bottom). We also present image data from a different cell imaging in the CMO channel that shows the location of the cell membrane (sarcolemma), see Fig. 4(b). Electrically induced contraction can be seen in both cells, see white arrows and white dashed line as a reference point to guide the eye. Orthogonal maximum intensity projections taken in the lab (X′, Y, Z′) coordinates of the same two cardiomyocytes are shown in Figs. 5(a) (Multimedia view) and 5(b) (Multimedia view), respectively. The calcium sparks can also be observed either in Figs. 5(c) and 5(d) or in the video of Fluo-4-labeled cardiomyocytes [see Fig. 5(a)]. Details of the image processing are provided in the supplementary material Sec. 11.

The results presented above demonstrate the first use of a DM for high-speed remote refocusing in LSFM volumetric imaging. The use of a DM for refocusing enables higher-order defocus terms to be applied in addition to the lowest order (quadratic) defocus compared to, e.g., the use of a liquid-tunable lens.[4] The approach also corrects for system aberrations. The use of a DM for remote refocusing in the detection arm also avoids the use of the polarizing beam splitter cube in LSFM systems employing the remote-refocusing approach of Sparks *et al.*[3] that reduces the collection efficiency of these systems.

The aperture of the DM reduced the overall detection NA to 0.72 and 0.75 in the horizontal and vertical directions, respectively, which was due to a sub-optimal magnification of the pair of relay tube lenses; the lenses used here were selected from the discrete range of focal lengths available commercially. In the future, this could be avoided

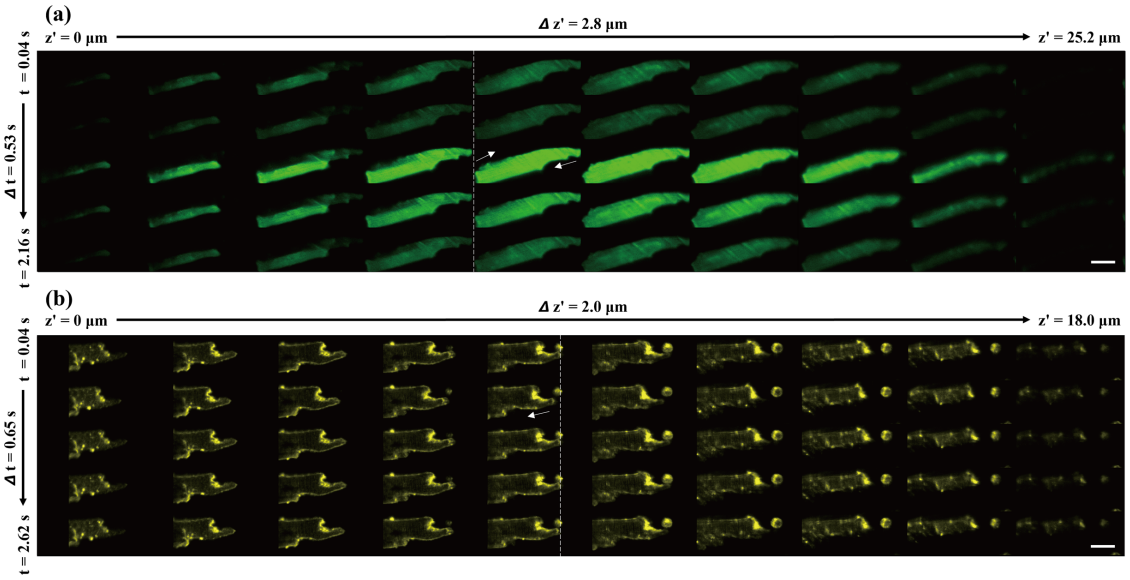

FIG. 4. Reconstructed ortho-sliced montage showing (a) Fluo-4 and (b) CMO 3D time-lapse data (X′Y view), respectively, for two different cardiomyocytes at 26.3 vps. Reference lines and arrows in (a) and (b) show the physical contraction of the cardiomyocytes. Scale bars, 20 μm.

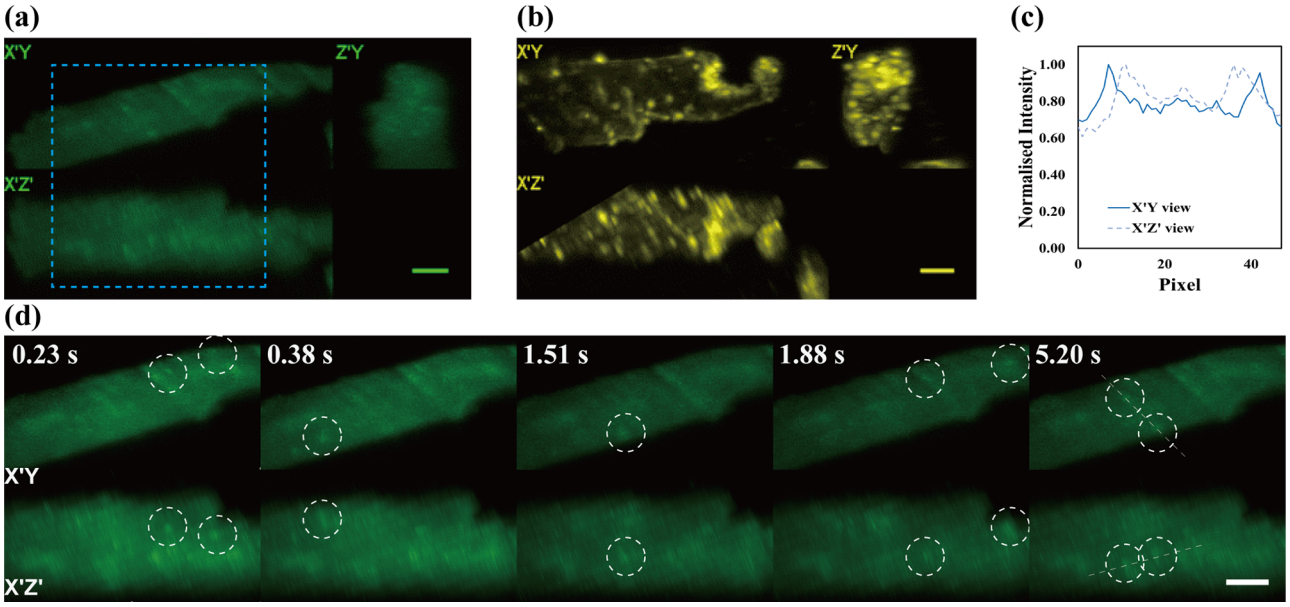

FIG. 5. Reconstructed three-view maximum intensity projections of (a) Fluo-4-labeled and (b) CMO-labeled cardiomyocytes. (c) The profiles of the calcium sparks along the dashed lines in (d) at $t = 5.20$ s. (d) The zoom-in time-lapse X′Y and X′Z′ maximum intensity images of the blue square region in (a) showing the calcium sparks in different time frames. The dashed white circles indicate the more distinct calcium spark events. Scale bars, 10 μm. Multimedia views: https://doi.org/10.1063/5.0125946.1; https://doi.org/10.1063/5.0125946.2

through the use of a relay with a magnification chosen to avoid clipping while still making the greatest possible use of the clear aperture of the DM, which may require the use of custom lenses or selected stock optics.[17] In addition, this system can be developed to achieve dual-channel fluorescence imaging and moved to a temperature-controlled lab to reduce the need to reoptimize the DM. The high reflectivity of the DM means that—apart from the slight clipping of the pupil—the system efficiently transmits the fluorescence collected by the detection objective to the camera, as compared to approaches that use a folded remote-refocusing system with polarization-based beam splitters.[3]

In light-sheet fluorescence microscopy, the imaging depth is limited by scattering and aberration of the illumination light sheet and by scattering and aberration of emitted fluorescence, both of which cause a decrease in image resolution and contrast with increasing depth. In the future, the imaging depth can be increased by incorporating line illumination and confocal slit detection[18] or by employing multiphoton excitation.[19]

The imaging speed achieved was limited by the frame rate of the camera for a useful number of pixels (1024×128 at 1290.8 fps). During optimization, we were also limited by the intensity available from the LED source used to illuminate the STM, as it was necessary to keep the illumination time short in order to avoid the motion of the DM blurring the image of the STM. Therefore, a higher speed camera and a more intense illumination source for optimization would be required in order to increase the achievable frame rate.

The maximum Strehl ratio achieved is above the diffraction limit for a refocus range of 60 μm, and the mean Strehl ratio over a 200×200 μm^2 region in sample space is above 0.6 over the whole refocus range of 50 to -50 μm. The spatial resolution was measured to be 0.51 ± 0.04 μm laterally and 2.24 ± 0.32 μm axially, and the sectioning strength was 3.71 ± 0.27 μm. We demonstrated the capabilities of the system in observing static pollen grain samples and dynamic electrically paced cardiomyocyte samples at 26.3 volumes per second with 35 usable frames per volume.

See the supplementary material for supporting content.

The authors would like to acknowledge funding from the British Heart Foundation (BHF, No. NH/16/1/32447). T.W. acknowledges a Ph.D. studentship funded by the Engineering and Physical Sciences Research Council. L.D. acknowledges an Engineering and Physical Sciences Research Council (EPSRC) and a BHF co-funded Ph.D. studentship (No. EP/L015498/1). The authors gratefully acknowledge the expert help from Martin Kehoe and Simon Johnson in the Optics Workshop of the Photonics Group of Imperial College London who helped fabricate the custom components for this high-speed LSFM system.

AUTHOR DECLARATIONS

Conflict of Interest

The authors have no conflicts to disclose.

Author Contributions

Wenzhi Hong: Formal analysis (equal); Investigation (equal); Methodology (equal); Software (equal); Visualization (equal); Writing – original draft (equal); Writing – review & editing (equal). **Terry Wright:** Investigation (equal); Methodology (equal); Software (equal); Writing – review & editing (equal). **Hugh Sparks:** Investigation (equal); Methodology (equal); Software (equal); Writing – review & editing

(equal). **Liuba Dvinskikh:** Investigation (equal); Methodology (equal); Writing – review & editing (equal). **Ken MacLeod:** Funding acquisition (equal); Methodology (equal); Supervision (equal); Writing – review & editing (equal). **Carl Paterson:** Conceptualization (equal); Funding acquisition (equal); Methodology (equal); Supervision (equal); Writing – review & editing (equal). **Christopher Dunsby:** Conceptualization (equal); Funding acquisition (equal); Methodology (equal); Supervision (equal); Writing – original draft (equal); Writing – review & editing (equal).

DATA AVAILABILITY

The data that support the findings of this study are openly available in Zenodo at https://doi.org/10.5281/zenodo.7007491, Ref. 20.

REFERENCES

[1]P. J. Keller, A. D. Schmidt, J. Wittbrodt, and E. H. Stelzer, "Reconstruction of zebrafish early embryonic development by scanned light sheet microscopy," Science **322**(5904), 1065–1069 (2008).

[2]E. J. Botcherby, R. Juskaitis, M. J. Booth, and T. Wilson, "Aberration-free optical refocusing in high numerical aperture microscopy," Opt. Lett. **32**(14), 2007 (2007).

[3]H. Sparks, L. Dvinskikh, J. M. Firth, A. J. Francis, S. E. Harding, C. Paterson *et al.*, "Development a flexible light-sheet fluorescence microscope for high-speed 3D imaging of calcium dynamics and 3D imaging of cellular microstructure," J. Biophotonics **13**(6), e201960239 (2020).

[4]F. O. Fahrbach, F. F. Voigt, B. Schmid, F. Helmchen, and J. Huisken, "Rapid 3D light-sheet microscopy with a tunable lens," Opt. Express **21**(18), 21010–21026 (2013).

[5]M. Duocastella, G. Sancataldo, P. Saggau, P. Ramoino, P. Bianchini, and A. Diaspro, "Fast inertia-free volumetric light-sheet microscope," ACS Photonics **4**(7), 1797–1804 (2017).

[6]T. Wright, H. Sparks, C. Paterson, and C. Dunsby, "Video-rate remote refocusing through continuous oscillation of a membrane deformable mirror," J. Phys. Photonics **3**(4), 045004 (2021).

[7]M. Zurauskas, O. Barnstedt, M. Frade-Rodriguez, S. Waddell, and M. J. Booth, "Rapid adaptive remote focusing microscope for sensing of volumetric neural activity," Biomed. Opt. Express **8**(10), 4369–4379 (2017).

[8]L. Streich, J. C. Boffi, L. Wang, K. Alhalaseh, M. Barbieri, R. Rehm *et al.*, "High-resolution structural and functional deep brain imaging using adaptive optics three-photon microscopy," Nat. Methods **18**(10), 1253–1258 (2021).

[9]M. R. Rai, C. Li, and A. Greenbaum, "Quantitative analysis of illumination and detection corrections in adaptive light sheet fluorescence microscopy," Biomed. Opt. Express **13**(5), 2960 (2022).

[10]Z. Qin, Z. She, C. Chen, W. Wu, J. K. Y. Lau, N. Y. Ip *et al.*, "Deep tissue multiphoton imaging using adaptive optics with direct focus sensing and shaping," Nat. Biotechnol. (published online 2022).

[11]U. Bitenc, N. A. Bharmal, T. J. Morris, and R. M. Myers, "Assessing the stability of an ALPAO deformable mirror for feed-forward operation," Opt. Express **22**(10), 12438–12451 (2014).

[12]J. Braat and P. Török, *Imaging Optics* (Cambridge University Press, 2019), pp. 582–656.

[13]V. Lakshminarayanan and A. Fleck, "Zernike polynomials: A guide," J. Mod. Opt. **58**(7), 545–561 (2011).

[14]J. Canny, "A computational approach to edge detection," IEEE Trans. Pattern Anal. Mach. Intell. **PAMI-8**(6), 679–698 (1986).

[15]M. Sato, P. O'Gara, S. E. Harding, and S. J. Fuller, "Enhancement of adenoviral gene transfer to adult rat cardiomyocytes *in vivo* by immobilization and ultrasound treatment of the heart," Gene Ther. **12**(11), 936–941 (2005).

[16]M. B. Sikkel, S. Kumar, V. Maioli, C. Rowlands, F. Gordon, S. E. Harding *et al.*, "High speed sCMOS-based oblique plane microscopy applied to the study of calcium dynamics in cardiac myocytes," J. Biophotonics **9**(3), 311–323 (2016).

[17]W. Hong and C. Dunsby, "Automatic tube lens design from stock optics for microscope remote-refocusing systems," Opt. Express **30**(3), 4274–4287 (2022).

[18]E. Baumgart and U. Kubitscheck, "Scanned light sheet microscopy with confocal slit detection," Opt. Express **20**(19), 21805–21814 (2012).

[19]T. V. Truong, W. Supatto, D. S. Koos, J. M. Choi, and S. E. Fraser, "Deep and fast live imaging with two-photon scanned light-sheet microscopy," Nat. Methods **8**(9), 757–760 (2011).

[20]W. Hong, T. Wright, H. Sparks, L. Dvinskikh, K. MacLeod, C. Paterson, and C. Dunsby (2022). "Dataset for adaptive light-sheet fluorescence microscopy with a deformable mirror for video-rate volumetric imaging," Zenodo, Dataset. https://doi.org/10.5281/zenodo.7007491